Journal of the Electrochemical Society

High-Capacity P2-Type $Na_xLi_{0.25}Mn_{0.75}O_2$ Cathode Enabled by Anionic Oxygen Redox

High-Capacity P2-Type $Na_xLi_{0.25}Mn_{0.75}O_2$ Cathode Enabled by Anionic Oxygen Redox

Xiaoli Chen,[1,2] Ning Li,[2] Elyse Kedzie,[3] Bryan D. McCloskey,[2,3,*] Haolin Tang,[1,z] and Wei Tong[2,*,z]

[1] *State Key Laboratory of Advanced Technology for Materials Synthesis and Processing, Wuhan University of Technology, Wuhan 430070, China*
[2] *Energy Storage and Distributed Resources Division, Lawrence Berkeley National Laboratory, Berkeley, California 94720, USA*
[3] *Department of Chemical and Biomolecular Engineering, University of California, Berkeley, California 94720, USA*

Sodium-ion battery technology has attracted significant attention due to its substantial cost advantage and similar operating mechanism to Li-ion batteries. P2-type sodium manganese oxide cathode is one of the most promising candidates, demonstrating both high capacity and good cycling stability. Here, we explore the lattice oxygen activity in layered sodium transition metal oxides. We synthesize a series of sodium lithium manganese oxides, $Na_xLi_{0.25}Mn_{0.75}O_2$ ($x = 0.75 - 0.833$), to optimize Na content. We further investigate the charge compensation mechanism for the best performing $Na_{0.75}Li_{0.25}Mn_{0.75}O_2$ over an extensive electrochemical cycling window. The large charge and discharge capacity is enabled by reversible lattice oxygen redox in the high voltage region ($\geq$2.5 V), along with Mn redox at the voltages below 2.5 V. Additionally, we reveal a small amount of oxygen gas evolution, 0.04% of the total oxygen in $Na_{0.25}Li_{0.25}Mn_{0.75}O_2$. This initial study will trigger an interest in the lattice oxygen activity in layered sodium metal oxide cathode, therefore, leading to better understanding of its correlation with crystal structure and electrochemical performance.

 [DOI: 10.1149/2.0611916jes]

Manuscript submitted October 8, 2019; revised manuscript received November 21, 2019. Published December 13, 2019.

Sodium-ion battery has attracted great attention as a potential alternative energy storage solution, especially for large-scale grid application, owing to the abundance of sodium and similarity to lithium-ion batteries.[1–6] The cathode is a critical component for the ultimate electrochemical performance of Na-ion cells. Layered sodium transition metal oxide has been considered as one of the most promising cathodes for advanced Na-ion batteries, given its outstanding rate capability.[7,8] Another advantage of the layered sodium transition metal oxide materials is the rich chemistry compared to the Li-ion analogs. For example, transition metals such as Fe and Cu, as well as the common Ni, Mn and Co, can be incorporated into the sodium layered structure. Moreover, sodium layered oxides can accommodate several types of crystal structure, of which O3- and P2-type structure (O and P represent octahedral and prismatic site for sodium ions and the number indicates the layer of transition metal in the unit cell) are the most common polymorphs. P2-type compounds with less Na content typically exhibit better capacity retention due to less phase transformation than O3-type analogs.[9]

Of many reported P2-type sodium cathodes, Mn-based sodium metal oxide is the most common chemistry because of its reasonably high cycling capacity and low cost. Continuous efforts have been made to improve the cycling performance by minimizing its irreversible phase transformation. One important strategy is to leverage its advantageous chemistry, thus allowing the incorporation of various dopants on the transition metal sites. For P2-type Na_xMnO_2 ($0.5 < x < 1$), the deintercalation of sodium ions relies on the oxidation of Mn^{3+} and Na^+ content. Motivation to further improve the cycling performance of sodium manganese oxide leads to an intense investigation of various dopants. Of interest are the low-valence metals such as monovalent Li, divalent Mg, and trivalent Al, Fe that reduce Mn^{3+} content and increase the Mn^{4+} content.[10,11] In an extreme case, P2-type $Na_{5/6}[Li_{1/4}Mn_{3/4}]O_2$, composed of $\frac{1}{12}$ Mn^{3+} and $\frac{11}{12}$ Mn^{4+}, can deliver a large reversible capacity of 200 mAh/g, far beyond the capacity relating to Mn^{3+}/Mn^{4+} redox.[10] Such a high capacity was attributed to the large contribution of the lattice oxygen redox reaction.[12,13]

In this work, we study the effect of alkali Na content on anionic oxygen activity in $Na_xLi_{0.25}Mn_{0.75}O_2$, including both reversible oxygen redox and irreversible oxygen loss. A series of $Na_xLi_{0.25}Mn_{0.75}O_2$ composition with x ranging from 0.75, where all Mn is 4+, to 0.87 are synthesized by a solid state reaction. Samples with Na content higher than 0.75 contain Mn^{3+}. Of all samples, the one with Na content of 0.75 delivers the highest reversible capacity of 231 mAh/g. We perform a detailed characterization on this compound via X-ray absorption spectroscopy (XAS) to understand the charge compensation mechanism in the bulk and at surface. Meanwhile, *operando* differential electrochemical mass spectrometry (DEMS) is employed to study the gas evolution behavior of this compound throughout the charge-discharge process.

Experimental

Material synthesis.—P2-type $Na_xLi_{0.25}Mn_{0.75}O_2$ ($x = 0.75$, 0.78, 0.833, and 0.87) were prepared by a solid-state reaction using Na_2CO_3, Li_2CO_3, and $MnCO_3$ as precursors. The starting materials were milled for 3 h, then heated at 700°C for 12 h in air.

Physical characterization.—Crystal structure was characterized on a Bruker D2 powder X-ray diffractometer (XRD, Cu Kα, 40 kV, 30 mA). Scanning electron microscopy (SEM) and energy dispersive X-ray spectroscopy (EDS) images were collected on a JEOL JSM-7500F field emission microscope at a 15 kV accelerating voltage. Samples for ex-situ characterization were harvested by opening the cycled cells at the designated cutoff voltages in an argon-filled glove box. Battery grade dimethyl carbonate (DMC) was used to wash away the electrolyte from the electrodes. After DMC solvent was fully evaporated, the electrode materials were sealed between the Kapton films to avoid any exposure to ambient atmosphere. Mn *K*-edge hard XAS measurements were conducted in the transmission mode using a (220) monochromator at SSRL beamline 4-1. For energy calibration, the peak of the first derivative of Mn foil was adjusted to the tabulated value of 6539 eV. X-ray absorption near-edge spectroscopy (XANES) data analysis was performed by SIXPACK software. Ex-situ soft XAS measurements were carried out in the total electron yield (TEY) mode under ultrahigh vacuum (10^{-9} torr) in a single load at room temperature using SSRL beamline 8-2.

Electrochemical characterization.—Electrochemical characterization was performed on a 2032-type coin cell. The electrode was prepared in an argon-filled glove box by mixing active material,

*Electrochemical Society Member.
[z]E-mail: weitong@lbl.gov; thln@whut.edu.cn

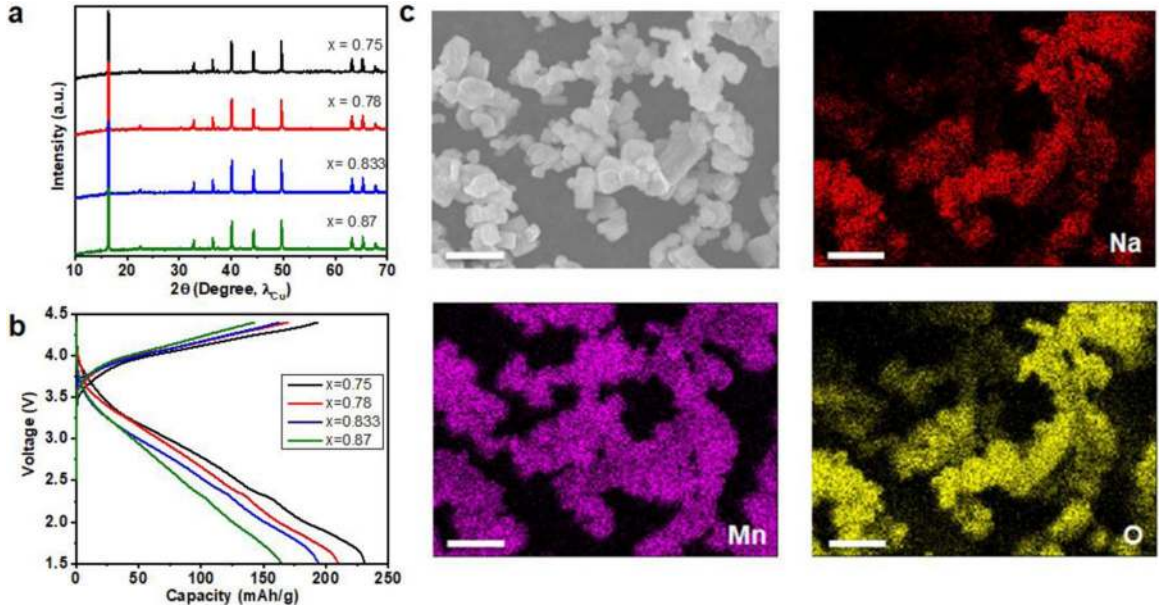

Figure 1. (a) XRD patterns; (b) the first charge-discharge voltage profiles of $Na_xLi_{0.25}Mn_{0.75}O_2$ (x = 0.75, 0.78, 0.8333, 0.87), cells are cycled between 4.4 and 1.5 V at C/20; and (c) morphology of and elemental distribution in $Na_{0.75}Li_{0.25}Mn_{0.75}O_2$.

acetylene black (Denka) and polyvinylidene fluoride (PVDF) binder (Kynar 2801) with a weight ratio of 80:10:10 on an aluminum foil. After dried at 120°C under vacuum for 12 h, cathode film was cut into the disks with an area of 1.27 cm^2 and typical loading of 2−3 mg/cm^2. Sodium foil (Sigma Aldrich) was used as the negative electrode, Whatman GF/D glass fiber as separators and 1 M $NaPF_6$ in ethylene carbonate (EC) and diethylene carbonate (DEC) with a volume ratio of 1:1 as the electrolyte. The coin cells were initially rested and equilibrated for 8 h before electrochemical testing. Galvanostatic charge-discharge was conducted between 1.5 and 4.4 V using a VMP3 multichannel potentiostat/galvanostat controlled by EC-Lab (BioLogic Science Instruments). 1C capacity is defined as 200 mAh/g. Cells were cycled at a constant current rate of C/20. For the galvanostatic intermittent titration technique (GITT) measurement, the cells were cycled at C/20 for 0.5 h followed by an open circuit relaxation for 1 h. The DEMS measurement was performed in a customized Swagelok-type cell with the same components as described above. DEMS cell was cycled at a constant current of 10 mA/g between 1.5 and 4.4 V. The cell was periodically pulsed with Ar gas at regular intervals to sweep the evolved gases from the headspace to the mass spectrometer for analysis.

Results and Discussion

Preliminary characterization of P2-type $Na_xLi_{0.25}Mn_{0.75}O_2$.—A series of samples, $Na_xLi_{0.25}Mn_{0.75}O_2$ (x = 0.75, 0.78, 0.83, and 0.87), are synthesized by a solid-state reaction. As shown in Figure 1a, all the samples are highly crystallized pure phases and the diffraction patterns are indexed well with P2-type phase (space group: P63/mmc).[10,14] From the SEM images (Figure S1), it can be seen that all the samples are composed of quite uniform particles with a hexagonal-plate shape and an average particle size of 1–4 μm. The first charge-discharge voltage profiles are presented in Figure 1b. Increasing Na content leads to a decrease in both charge and discharge capacity during the first cycle. Indeed, the capacity of P2-type cathode strongly depends on the composition. The most direct relevance is the presence of the Jahn-Teller Mn^{3+} cation that affects the energy barrier for Na^+ hopping as well as Na^+ conduction.[15,16] A higher polarization is observed for phases with Na content above 0.75. Of all the samples, the one with x = 0.75 delivers the highest initial charge and discharge capacity of 193 and 232 mAh/g, corresponding to 0.66 and 0.79 Na^+, respectively. According to the EDS analysis, the best performing $Na_{0.75}Li_{0.25}Mn_{0.75}O_2$ sample exhibits uniform elemental distribution of Na, Mn and O.

Electrochemical characterization of $Na_{0.75}Li_{0.25}Mn_{0.75}O_2$.—A detailed electrochemical characterization is carried out on $Na_{0.75}Li_{0.25}Mn_{0.75}O_2$. Figure 2a shows the charge-discharge voltage profiles during the first 20 cycles at C/20 and representative dQ/dV curves are presented in Figure 2b. The first charge profile of $Na_{0.75}Li_{0.25}Mn_{0.75}O_2$ is characterized by a relatively flat plateau, completely different from the discharge profiles, which are featured by a more sloping curve in the high voltage region and two small plateaus below 2.5 V. The anodic and cathodic peaks and their evolution upon cycling are more visible in the dQ/dV plots. The high voltage region shows one anodic peak around 4.0 V and several small cathodic peaks around 3.9, 3.5 and 3.1 V, while two pairs of anodic/cathodic peaks around 2.5 and 2.1 V dominate the low voltage region. Upon repeated cycling, the shape of charge-discharge profiles is mostly retained, but the reversible capacity gradually drops from the initial 232 mAh/g to 144 and 134 mAh/g at the 20th and 50th cycle, respectively (Figure 2c). Such capacity drop largely originates from the high-voltage redox during charging and low-voltage redox at 2.0 V during discharging. As discussed earlier, Mn in $Na_{0.75}Li_{0.25}Mn_{0.75}O_2$ should be tetravalent in order to achieve charge balance. In principle, it is difficult to oxidize to Mn^{5+} because Mn^{5+} is not stable in octahedral coordination, but usually in tetrahedral coordination according to the ligand field theory. The splitting of *d* orbital energy levels by an octahedral field is larger compared to that by a tetrahedral field. Additionally, the structure of octahedral splitting levels is inverted with respect to that of the tetrahedral splitting. The ligand field splitting caused by octahedral coordination is stronger, therefore, more difficult to oxidize octahedral Mn^{4+} to octahedral Mn^{5+}.[17] Therefore, the only element that contributes the electron upon desolidation would be oxygen. Upon discharging, the possible redox-active species that can contribute to the high capacity are oxygen and Mn, of which Mn can be reduced from Mn^{4+} to Mn^{3+}/Mn^{2+}, depending on the discharge cutoff voltage. The detailed charge compensation mechanism will be discussed in the next section. We conduct GITT test to probe the kinetics of different redox at different states of charge (Figure 2d). Overall, $Na_{0.75}Li_{0.25}Mn_{0.75}O_2$ exhibits a quite constant polarization during the charge, which mostly represents the kinetics of sole oxygen oxidation reaction in $Na_{0.75}Li_{0.25}Mn_{0.75}O_2$. During the discharge, a slightly higher polarization is revealed, probably relating to the solid electrolyte interface (SEI) formation at high voltages during charge. The kinetics toward the end of discharge is slightly lower than that in the high voltage region, suggesting the existence of different redox

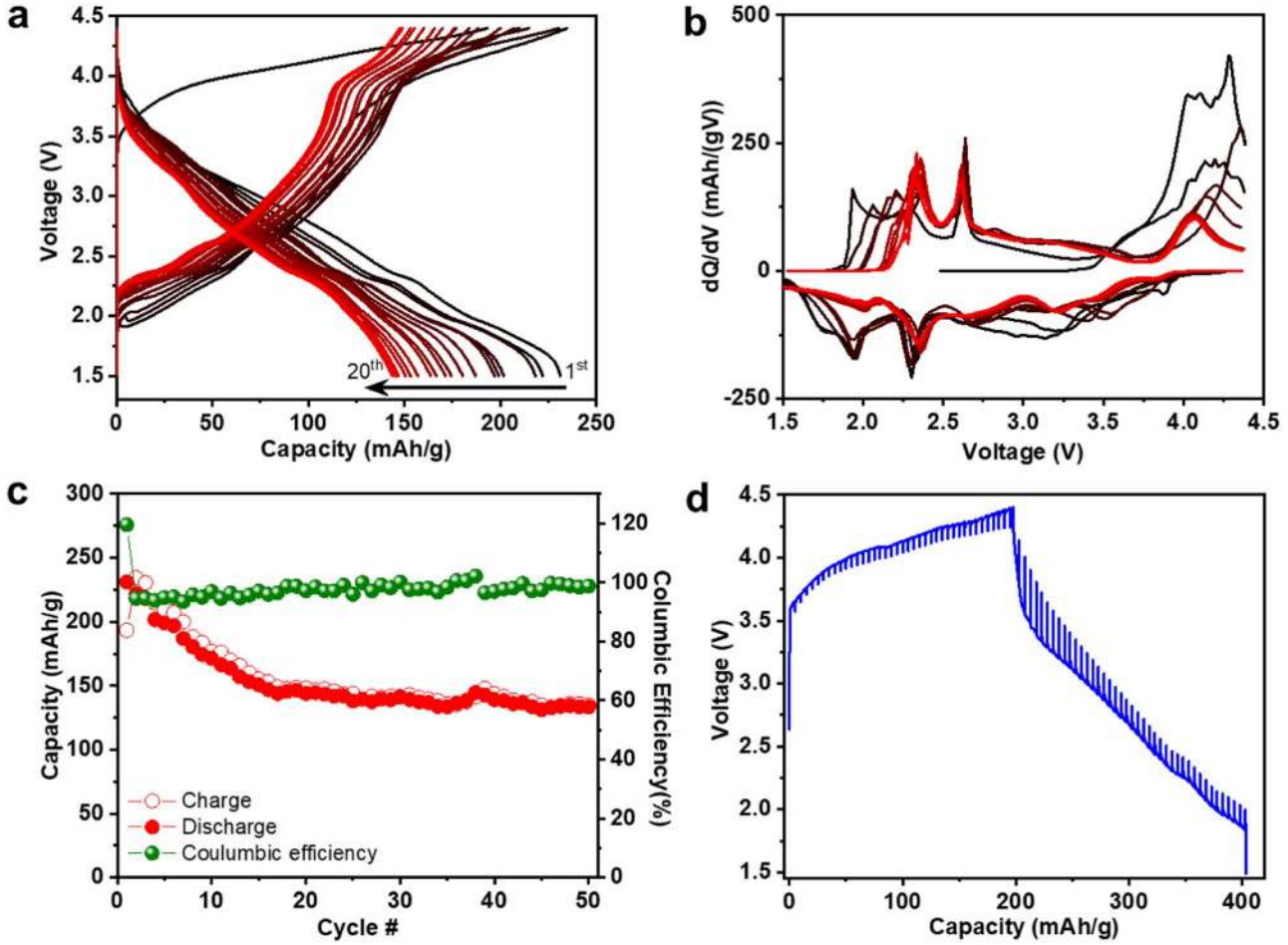

Figure 2. (a) Charge-discharge voltage profiles, (b) dQ/dV plots, (c) cycling performance and (d) GITT curve of $Na_{0.75}Li_{0.25}Mn_{0.75}O_2$.

chemistry (i.e., O vs. Mn). We notice that they are generally comparable, in contrast to the largely differed kinetics between O and Ni redox observed in Li-ion metal oxide cathode.

It is known that P2-type sodium manganese oxide undergoes complex phase transition at high voltage/low Na content, where P2 to O2 transition is particularly detrimental.[18,19] However, doping Li in the transition metal layer can largely inhibit the phase transition.[13] Here, we investigate the structural change of $Na_{0.75}Li_{0.25}Mn_{0.75}O_2$ phase during the initial charge and discharge process via collecting ex-situ XRD patterns at different states of charge (Figure 3). Consistent with previous report,[13] a predominant solid solution phase evolution is revealed during the first cycle. It should be noted that it is possible to extract Li^+ from the material upon charging. From ex-situ XRD, the diffraction peak at 14° (λ = 0.97625 Å) relating to the long-range in-plane ordering between Li and Mn ions starts to diminish at highly charged states. Yang et al. probed the local environment of Li upon cycling via nuclear magnetic resonance study, showing partially reversible Li extraction/insertion during charge/discharge improves cycling performance.[20] Subtle change in the local structure is possible based on the multiple pairs of redox peaks revealed by the dQ/dV curves. Further investigation of the local structure at the microscopic scale will be helpful in this context.

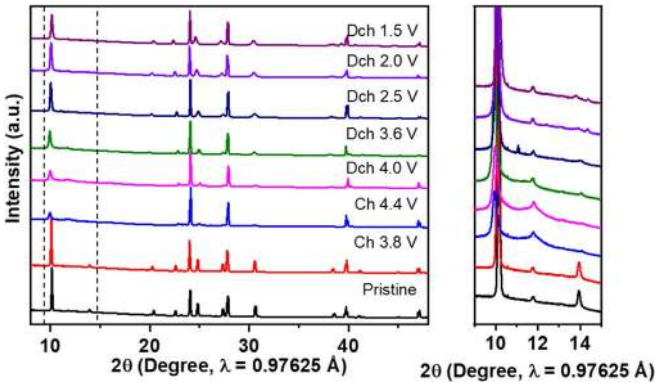

Figure 3. Ex-situ XRD patterns of $Na_{0.75}Li_{0.25}Mn_{0.75}O_2$ at different states of charge. The cells are cycled between 4.4 and 1.5 V at C/20.

Charge compensation mechanism.—The electronic structure of Mn in the bulk and at the surface of $Na_{0.75}Li_{0.25}Mn_{0.75}O_2$ during the first charge and discharge process is investigated at different states of charge using combined hard and soft XAS. Mn *K*-edge spectra upon charging and discharging are shown in Figs. 4a, 4b along with Mn_2O_3 and MnO_2 reference. Upon desodiation, the energy shift of Mn *K*-edge at the half maxima is consistent with that MnO_2, indicating Mn^{4+} at prisitine state. Upon charging (Figure 4a), it displays no noticeable energy shift, confirming that Mn remains as 4+ upon continuous desodiation. Therefore, only O participates in the electrochemical oxidation upon charging. During the discharge process, there is no further change in the energy shift of Mn *K*-edge until 2.5 V discharge, indicating the oxygen redution contributes to the capacity at discharge above 2.5 V, in good agreement with the GITT result. Further discharging to 1.5 V, Mn *K*-edge shows a shift to a lower energy, indicating the reduction of Mn^{4+}. It is worth noting that the average oxidation state of Mn is higher than 3+, suggesting no complete redution of Mn^{4+} in $Na_{0.75}Li_{0.25}Mn_{0.75}O_2$ at the end of discharge.

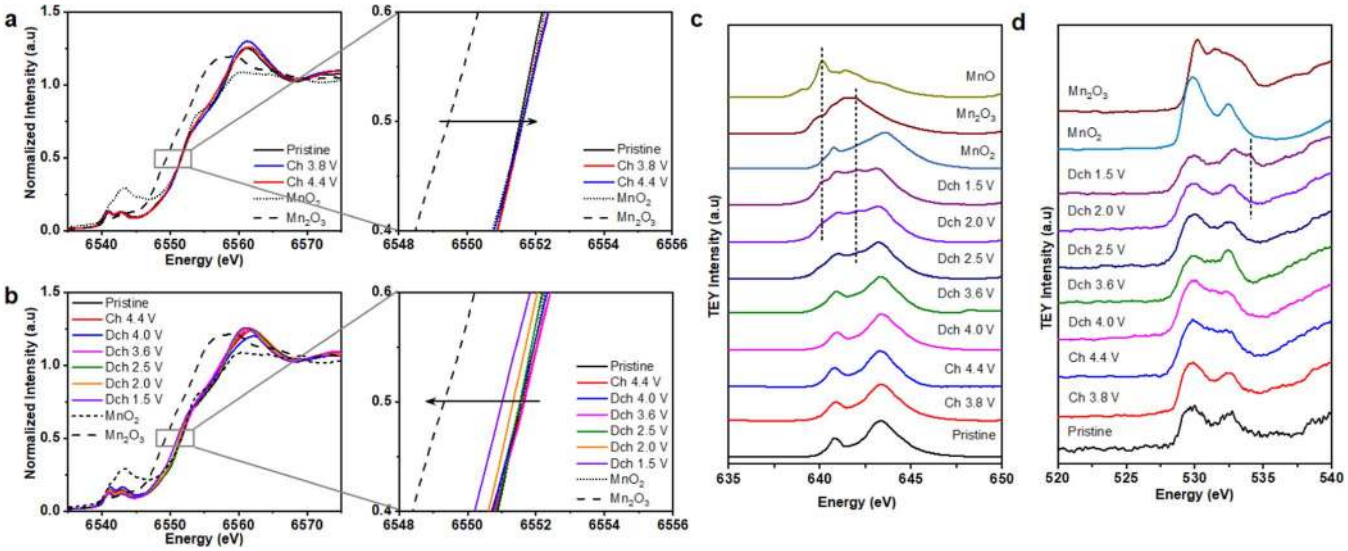

Figure 4. XANES Mn K-edge (a) during the charge and (b) during the discharge, soft XAS (c) Mn L-edge and (d) O K-edge of $Na_{0.75}Li_{0.25}Mn_{0.75}O_2$ at different states of charge. Dash lines in (c) and (d) highlight the features of Mn^{3+}, Mn^{2+} and carbonate toward the end of discharge, respectively.

We further examine the electronic structure of Mn at the surface by using the total electron yield (TEY) mode of soft XAS with a probing depth of 2–5 nm.[21–23] Mn *L*-edge spectra (Figure 4c) at pristine and charged states is consistent with that of MnO_2 reference, suggesting Mn^{4+} at the surface during charge, even at the high voltages. This observation is very intriguing compared to its Li analogs, which typically shows transition metal reduction at high delithiation states when charged to high voltages.[24,25] At the beginning of the discharge process (≥3.6 V), there is no change in Mn *L*-edge. Starting from 2.5 V discharge, we observe the evolution of an additional shoulder around 640.1 eV, which signifies the formation of Mn^{3+} and Mn^{2+} at the surface toward the end of discharge. Close comparison with the Mn *L*-edge of Mn^{4+}, Mn^{3+} and Mn^{2+} reference, we estimate a large portion of Mn^{4+} still remains at the end of discharge. Clearly, the capacity in the low voltage region (<2.5 V) is contributed by combined Mn^{4+}/Mn^{3+} and Mn^{3+}/Mn^{2+} redox, therefore, the loss of Mn redox possibly accounts for the capacity fade around 2 V. Meanwhile, soft XAS O *K*-edge spectra (Figure 4d) reveals the formation of a trace amount of carbonate at 1.5 V discharge.[26,27]

Overall, a considerable amount of oxygen oxidation occurs in $Na_{0.75}Li_{0.25}Mn_{0.75}O_2$ during the charge process, given the total 0.66 Na^+ extraction. More importantly, such oxygen redox reaction seems quite reversible. Although Mn reduction at < 2.5 V discharge is observed, the contribution of low-voltage Mn redox is small according to our XAS results, showing a small amount of reduced Mn at the end of discharge.

Gas evolution from $Na_{0.75}Li_{0.25}Mn_{0.75}O_2$.—Because Na^+ removal is accompanied by oxygen oxidation during the initial charge of $Na_{0.75}Li_{0.25}Mn_{0.75}O_2$, we examine the gas evolution behavior, due to the exposure to the liquid electrolyte at high operating voltages, during the electrochemical cycling. The *operando* DEMS results are shown in Figure 5. The DEMS cell is cycled at a current density of 20 mA/g. CO_2 gas evolution occurs continuously during the charge process, showing a faster release at > 4.2 V before a quite steady release at the low voltages. CO_2 evolution at the initial stage of charge mostly originates from the residual carbonate during the synthesis,[28–30] as well as the side reactions with electrolyte at the high voltages.[31,32] Meanwhile, O_2 evolution is not detected until 4.1 V charge. The total amount of CO_2 and O_2 released from the $Na_{0.75}Li_{0.25}Mn_{0.75}O_2$ cell during the first cycle is 0.628 and 0.0535 μmol, corresponding to a maximum of 0.5% and 0.04% total O in $Na_{0.75}Li_{0.25}Mn_{0.75}O_2$, if we assume all O is contributed by the active material. From the *operando* DEMS results, irreversible oxygen release occurs, but the extent is minimal in $Na_{0.75}Li_{0.25}Mn_{0.75}O_2$, which is consistent with Mn^{4+} (no reduction) at 4.4 V charge revealed by XAS.

Note the oxygen evolution behavior is quite different compared to its layered lithium analogs, which is much higher (i.e., 2.8% total O in $Li_{1.2}Ni_{0.2}Mn_{0.6}O_2$).[24,33] In Li-rich layered oxide, the irreversible oxygen loss results in the transition metal reduction at the surface, which presents a serious concern for the practical use of oxygen redox in Li-ion cells. Here, the results clearly reveal different oxygen activity in P2-type layered sodium metal oxide, the contrast may originate from the relatively stable local environment of oxygen in P2-type structure.

Conclusions

P2-type layered sodium transition metal oxides, $Na_xLi_{0.25}Mn_{0.75}O_2$, at a series of Na contents (x values) are synthesized by a solid-state reaction. We find the optimal Na content for this series of P2-type compounds is 0.75 when all Mn is tetravalent, which displays the highest initial charge and discharge capacity. The charge capacity originates from the oxygen oxidation reaction and a large portion of lattice oxygen redox is reversible upon discharging,

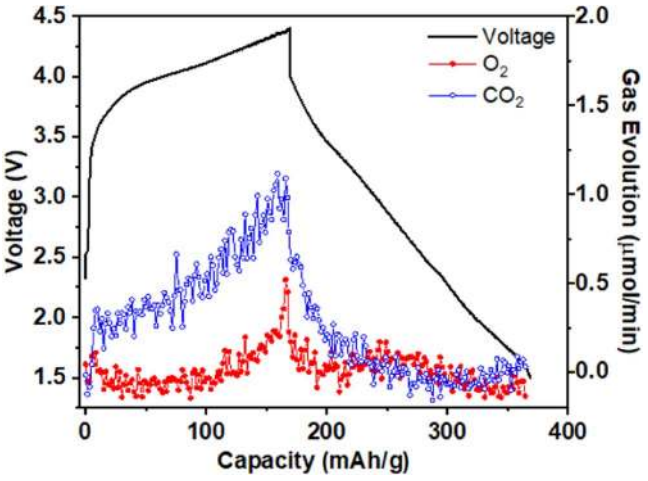

Figure 5. Gas evolution of $Na_{0.75}Li_{0.25}Mn_{0.75}O_2$ by the operando DEMS. The cell composed of 11.84 mg active material (128.45 μmol) is cycled at C/20 between 4.4 and 1.5V.

while Mn redox appears to contribute to capacity in the low voltage region (<2.5 V). Both CO_2 and O_2 gas evolution is detected by the operando DEMS during the first cycle, but the oxygen release only accounts for 0.04% total oxygen in $Na_{0.75}Li_{0.25}Mn_{0.75}O_2$ active material. This work serves to benchmark the reversible anionic oxygen redox and irreversible oxygen loss behavior in layered sodium lithium manganese oxide cathode. Further investigation of the key factors that govern the oxygen oxidation and its reversible behavior in sodium transition metal oxide cathode is needed for the practical utilization of oxygen redox in advanced Na-ion battery cathode.

Acknowledgments

X.C. appreicates the scholarship from the China Scholarship Council. The authors thank the support from the Assistant Secretary for Energy Efficiency and Renewable Energy, Office of Vehicle Technologies of the U.S. Department of Energy under Contract No. DE-AC02-05CH11231 and Energy & Biosciences Institute through the EBI-Shell program. Use of the Stanford Synchrotron Radiation Lightsource, SLAC National Accelerator Laboratory, is supported by the U.S. Department of Energy, Office of Science, Office of Basic Energy Sciences under Contract No. DE-AC02-76SF00515. The authors thank Dr. Marca Doeff at Lawrence Berkeley National Laboratory for the initiation of this work and Dr. Hui Xiong at Boise State University for useful advice on electrolyte preparation.

ORCID

Bryan D. McCloskey https://orcid.org/0000-0001-6599-2336
Wei Tong https://orcid.org/0000-0002-2878-1297

References

1. S.-W. Kim, D.-H. Seo, X. Ma, G. Ceder, and K. Kang, *Adv. Energy Mater.*, **2**, 710 (2012).
2. N. Yabuuchi, K. Kubota, M. Dahbi, and S. Komaba, *Chem. Rev.*, **114**, 11636 (2014).
3. J. Y. Hwang, S. T. Myung, and Y. K. Sun, *Chem. Soc. Rev.*, **46**, 3529 (2017).
4. X. Zheng, C. Bommier, W. Luo, L. Jiang, Y. Hao, and Y. Huang, *Energy Storage Mater.*, **16**, 6 (2019).
5. C. Delmas, *Adv. Energy Mater.*, **8**, 1703137 (2018).
6. J. Xu, F. Lin, M. M. Doeff, and W. Tong, *J. Mater. Chem. A*, **5**, 874 (2017).
7. I. Hasa, S. Passerini, and J. Hassoun, *J. Mater. Chem. A*, **5**, 4467 (2017).
8. A. Konarov, J. H. Jo, J. U. Choi, Z. Bakenov, H. Yashiro, J. Kim, and S.-T. Myung, *Nano Energy*, **59**, 197 (2019).
9. E. Talaie, V. Duffort, H. L. Smith, B. Fultz, and L. F. Nazar, *Energy Environ. Sci.*, **8**, 2512 (2015).
10. N. Yabuuchi, R. Hara, M. Kajiyama, K. Kubota, T. Ishigaki, A. Hoshikawa, and S. Komaba, *Adv. Energy Mater.*, **4**, 1301453 (2014).
11. B. Song, E. Hu, J. Liu, Y. Zhang, X.-Q. Yang, J. Nanda, A. Huq, and K. Page, *J. Mater. Chem. A*, **7**, 1491 (2019).
12. C. Zhao, Q. Wang, Y. Lu, L. Jiang, L. Liu, X. Yu, L. Chen, B. Li, and Y.-S. Hu, *Energy Storage Mater.* (2018).
13. X. Rong, E. Hu, Y. Lu, F. Meng, C. Zhao, X. Wang, Q. Zhang, X. Yu, L. Gu, Y.-S. Hu, H. Li, X. Huang, X.-Q. Yang, C. Delmas, and L. Chen, *Joule*, **3**, 503 (2019).
14. L. Yang, X. Li, X. Ma, S. Xiong, P. Liu, Y. Tang, S. Cheng, Y.-Y. Hu, M. Liu, and H. Chen, *J. Power Sources*, **381**, 171 (2018).
15. R. J. Clément, P. G. Bruce, and C. P. Grey, *J. Electrochem. Soc.*, **162**, A2589 (2015).
16. G. J. Shu and F. C. Chou, *Phys. Rev. B*, **78**, 052101 (2008).
17. J. A. Saint, M. M. Doeff, and J. Reed, *J. Power Sources*, **172**, 189 (2007).
18. S. Kumakura, Y. Tahara, K. Kubota, K. Chihara, and S. Komaba, *Angew. Chem. Int. Ed.*, **55**, 12760 (2016).
19. K. Kubota, S. Kumakura, Y. Yoda, K. Kuroki, and S. Komaba, *Adv. Energy Mater.*, **8**, 1703415 (2018).
20. L. Yang, X. Li, J. Liu, S. Xiong, X. Ma, P. Liu, J. Bai, W. Xu, Y. Tang, Y.-Y. Hu, M. Liu, and H. Chen, *J. Am. Chem. Soc.*, **141**, 6680 (2019).
21. C. Tian, Y. Xu, D. Nordlund, F. Lin, J. Liu, Z. Sun, Y. Liu, and M. Doeff, *Joule*, **2**, 464 (2018).
22. Won-Sub Yoon, Mahalingam Balasubramanian, Kyung Yoon Chung, Xiao-Qing Yang, James McBreen, and P Clare, Grey and D. A. Fischer, *J. Am. Chem. Soc.*, **127**, 17479 (2005).
23. F. Lin, I. M. Markus, D. Nordlund, T. C. Weng, M. D. Asta, H. L. Xin, and M. M. Doeff, *Nat. Commun.*, **5**, 3529 (2014).
24. J. Xu, M. Sun, R. Qiao, S. E. Renfrew, L. Ma, T. Wu, S. Hwang, D. Nordlund, D. Su, K. Amine, J. Lu, B. D. McCloskey, W. Yang, and W. Tong, *Nat. Commun.*, **9**, 947 (2018).
25. J. Xu, E. Hu, D. Nordlund, A. Mehta, S. N. Ehrlich, X.-Q. Yang, and W. Tong, *ACS Appl. Mater. Interfaces*, **8**, 31677 (2016).
26. R. Qiao, Y. D. Chuang, S. Yan, and W. Yang, *PLoS One*, **7**, e49182 (2012).
27. T. Risthaus, D. Zhou, X. Cao, X. He, B. Qiu, J. Wang, L. Zhang, Z. Liu, E. Paillard, G. Schumacher, M. Winter, and J. Li, *J. Power Sources*, **395**, 16 (2018).
28. U. Maitra, R. A. House, J. W. Somerville, N. Tapia-Ruiz, J. G. Lozano, N. Guerrini, R. Hao, K. Luo, L. Jin, M. A. Perez-Osorio, F. Massel, D. M. Pickup, S. Ramos, X. Lu, D. E. McNally, A. V. Chadwick, F. Giustino, T. Schmitt, L. C. Duda, M. R. Roberts, and P. G. Bruce, *Nat. Chem.*, **10**, 288 (2018).
29. Roland Jung, Michael Metzger, Filippo Maglia, Christoph Stinner, and A Hubert, Gasteigera, *J. Electrochem. Soc.*, **164**, A1361 (2017).
30. S. E. Renfrew and B. D. McCloskey, *J. Am. Chem. Soc.*, **139**, 17853 (2017).
31. K. Luo, M. R. Roberts, R. Hao, N. Guerrini, D. M. Pickup, Y. S. Liu, K. Edstrom, J. Guo, A. V. Chadwick, L. C. Duda, and P. G. Bruce, *Nat. Chem.*, **8**, 684 (2016).
32. R. Jung, M. Metzger, F. Maglia, C. Stinner, and H. A. Gasteiger, *J. Phys. Chem. Lett.*, **8**, 4820 (2017).
33. J. Xu, S. Renfrew, M. A. Marcus, M. Sun, B. D. McCloskey, and W. Tong, *J. Phys. Chem. C*, **121**, 11100 (2017).